



HAL
open science

Super-resolution imaging of antibody-conjugated biodegradable periodic mesoporous organosilica nanoparticles for targeted chemotherapy of prostate cancer

Pradip Das, Silvia Pujals, Lamiaa M A Ali, Magali Gary-Bobo, Lorenzo Albertazzi, Jean-Olivier Durand

► To cite this version:

Pradip Das, Silvia Pujals, Lamiaa M A Ali, Magali Gary-Bobo, Lorenzo Albertazzi, et al.. Super-resolution imaging of antibody-conjugated biodegradable periodic mesoporous organosilica nanoparticles for targeted chemotherapy of prostate cancer. *Nanoscale*, 2023, 15 (28), pp.12008-12024. 10.1039/D3NR01571H . hal-04179249

HAL Id: hal-04179249

<https://hal.science/hal-04179249v1>

Submitted on 9 Aug 2023

HAL is a multi-disciplinary open access archive for the deposit and dissemination of scientific research documents, whether they are published or not. The documents may come from teaching and research institutions in France or abroad, or from public or private research centers.

L'archive ouverte pluridisciplinaire **HAL**, est destinée au dépôt et à la diffusion de documents scientifiques de niveau recherche, publiés ou non, émanant des établissements d'enseignement et de recherche français ou étrangers, des laboratoires publics ou privés.



Distributed under a Creative Commons Attribution 4.0 International License

Super-resolution Imaging of Antibody Conjugated Biodegradable Periodic Mesoporous Organosilica Nanoparticles for Targeted Chemotherapy of Prostate Cancer

Pradip Das,* Silvia Pujals,* Lamiaa M. A. Ali, Magali Gary-Bobo, Lorenzo Albertazzi, Jean-Olivier Durand

P. Das, J.-O. Durand

ICGM, Univ. Montpellier, CNRS, ENSCM, Montpellier 34293, France

daspradip43@gmail.com

P. Das, S. Pujals, L. Albertazzi

Nanoscopy for Nanomedicine Group, Institute for Bioengineering of Catalonia (IBEC),
Barcelona 08036, Spain

silvia.pujals@iqac.csic.es

L.M.A. Ali, M. Gary-Bobo

IBMM, Univ. Montpellier, CNRS, ENSCM, 34093 Montpellier, France

Keywords

nanoPMOs, surface functionality, biodegradation, dSTORM imaging, drug delivery, targeted chemotherapy, prostate cancer

Abstract: Biodegradable periodic mesoporous organosilica nanoparticles (nanoPMOs) are widely used as responsive drug delivery platforms for targeted chemotherapy of cancer. However, the evaluation of their properties such as surface functionality and biodegradability is still challenging, which has a significant impact on the efficiency of chemotherapy. In this

study, we use direct stochastic optical reconstruction microscopy (dSTORM), a single molecule super-resolution microscopy technique, to quantify the degradation of nanoPMOs triggered by glutathione and the multivalency of antibody-conjugated nanoPMOs. Subsequently, the effect of these properties on cancer cell targeting, drug loading and release capability, and anticancer activity is also studied. Due to the higher spatial resolution at the nanoscale, dSTORM imaging is able to reveal the structural properties (i.e. size and shape) of fluorescent and biodegradable nanoPMOs. The quantification of nanoPMOs biodegradation using dSTORM imaging demonstrates their structure-dependent excellent degradation behavior at a higher glutathione concentration. The surface functionality of anti-M6PR antibody-conjugated nanoPMOs as quantified by dSTORM imaging exhibit a key role in prostate cancer cell labeling: oriented antibody is more effective than random ones while high multivalency is also effective. The higher biodegradability and cancer cell targeting properties of nanorod conjugated with oriented antibody (EAB4H) effectively deliver the anticancer drug doxorubicin to cancer cells, exhibiting potent anticancer effects.

1. Introduction

Cancer has become a major threat to human health, resulting in higher mortality rates worldwide in recent years.^[1] Among various kinds of therapeutic approaches, chemotherapy is often applied for cancer treatment in the clinic.^[2] However, anticancer drugs such as doxorubicin used in chemotherapy also damage healthy cells significantly, leading to a variety of adverse side effects observed in patients.^[3] To minimize the typical limitations of chemotherapeutic agents, various nanoparticle-based drug delivery systems have been investigated in both preclinical and clinical studies.^[4] Although high accumulation of these nanoscale delivery systems in tumor sites by the enhanced permeability and retention (EPR) effect improves the antitumor efficiency of chemotherapeutics,^[5] the significant nonspecific uptake of nanoparticles in healthy organs including the liver and spleen, followed by long-

term accumulation in the body, causes serious health problems.^[6] In light of this, the utilization of biodegradable nanomaterials with the tumor-targeting strategy has paid more attention to the development of potent nanomedicine for targeted and responsive drug delivery to further improve the therapeutic index as well as reduce the side effects.^[4a, 5b, 7]

The degradability characteristics of drug delivery nanoplateforms by external and/or internal stimuli allow the chemotherapeutics to be released in a controlled manner, reducing side effects.^[7-8] Furthermore, the biodegradability of nanoparticles especially inorganic nanoparticles significantly benefits clearing them from the body after performing the action within a specified time frame, reducing the toxicity caused by long-term accumulation.^[6, 7b, 9] In drug delivery applications, biodegradable periodic mesoporous organosilica nanoparticles (nanoPMOs) derived from organosilane are therefore acting as excellent nanocarriers thanks to their exceptional properties like tunable porosity and high biocompatibility. Despite the availability of different stimuli such as pH, light, and redox, the design of biodegradable nanoPMOs *via* simply incorporating disulfide or tetrasulfide linkages is mostly devoted to preclinical studies for taking the advantage of enormous concentration variation of glutathione (GSH) in extracellular (2-10 μ M) and intracellular (2-10 mM) tumor environments. As a result, appropriately designed nanoPMOs are significantly degraded into small fragments by elevated glutathione level present in the reduced form in tumor cells, resulting in drug release and clearance.^[10] To understand the biodegradation of nanoPMOs triggered by reduced glutathione, transmission electron microscopy (TEM) is the most commonly used so far, with the advantage of very high resolution, but which provides qualitative information only.^[10g] Since the degradation rate of nanoPMOs is extremely influenced by their inherent physicochemical properties including composition and porosity, thus quantitative analysis is crucial to optimize the properties of nanoPMOs for efficient cancer chemotherapy. Therefore, we have involved first-time a single molecule super-resolution microscope technique at 20 nm

resolution scale, direct stochastic optical reconstruction microscopy (dSTORM) for the quantification of nanoPMOs degradation in this study.

To improve the therapeutic performance of chemotherapy, the current preclinical/clinical research is focused on the targeted delivery^[11] of chemotherapeutics using surface-engineered nanoparticles which becomes more popular in increasing their accumulation in tumor cells/tissues effectively and specifically, exhibiting potent anticancer activity which also benefits the redox-responsive drug delivery.^[12] This can be easily achieved by the functionalization of the nanoparticle's surface with different biomolecules including peptides, aptamers, and antibodies which have specific interactions with particular cell surface receptors overexpressed on cancer cells.^[13] With our aim of developing more effective targeted and responsive chemotherapy for prostate cancer which has the overexpression of mannose-6-phosphate receptor (M6PR),^[14] biodegradable nanoPMOs are conjugated with anti-M6PR antibody because of its higher specificity and binding affinity compared to small molecules.^[15] Notably, the nature of surface functionality of nanoparticles (e.g., orientations and density of biomolecules) in addition to their structural properties play a pivotal role in their cellular internalization and subsequent intracellular fate, thus affecting the therapeutic efficiency.^[16] Therefore, the evaluation of the surface functionality of nanoparticles is one of the most important steps for the development of potent nanomedicine with a future perspective in clinical applications.^[17] Nevertheless, the accurate quantification of such biomolecules conjugated to each nanoparticle's surface (i.e. nanoparticle multivalency) by conventional assays using low-sensitive instruments is challenging so far,^[18] which becomes more complicated when the molar concentration of the nanoparticle cannot be easily determined with high accuracy and precision.^[19] Recently, our research group has been investigating the surface functionality to better understand the distribution/orientation/number of targeting ligand present at a single particle level by the single-molecule dSTORM imaging

technique.^[20a, 20b] Herein, we have studied a new class of materials known as nanoPMOs which have a high potential for targeted drug delivery.

dSTORM have been reported to enable the imaging of single biomolecules such as oligonucleotides and antibodies within NPs at a molecular scale which allows clear visualizing their distribution as well as quantification conjugated to nanoparticles, measuring the surface functionality of multivalent nanoparticles and tracking their interaction with cellular components.^[21] Hence, dSTORM multiplexing imaging is exploited here for qualitative and quantitative characterization of biodegradable nanoPMOs and analysis of functionalization with anti-M6PR antibody to reach a higher level of therapeutic efficiency in targeted chemotherapy of prostate cancer. In this work, we have synthesized and well-characterized a library of fluorescent and biodegradable nanoPMOs with varied sizes, shapes, compositions, in order to investigate their physicochemical properties predominantly biodegradability by super-resolution dSTORM imaging modality for effective stimuli-responsive drug delivery. In order to target prostate cancer, nanoPMOs were conjugated to anti-M6PR antibody either using EDC-NHS or semicarbazone chemistries, which lead to a random orientation or an oriented immobilization of the antibody respectively on the surface of nanoPMOs. In dSTORM imaging with nanometric spatial resolution (around 20 nm), we have quantified the biodegradation of various nanoPMOs at higher glutathione levels and found that their excellent degradation behavior depends on their structural characteristics. A single particle level analysis of nanoPMOs conjugated with an anti-M6PR antibody has revealed that one of the most important parameters, namely the surface functionality of nanoPMOs, such as the number, distribution, and density of antibody per nanoparticle, shows a significant impact on prostate cancer cell targeting using dSTORM imaging. Aside from the surface functionality of nanoPMOs, the size, and shape of nanoPMOs also significantly influence their interaction with living cells, leading to variations in cellular uptake by healthy

and cancerous prostate cells. According to the results, small-sized nanorods functionalized with oriented antibody have higher M6PR overexpressed prostate cancer cell labeling capabilities when they are functionalized at high density, whereas heterogeneous surface functionality reduces the ability of nanoPMOs with low multivalency to bind to cancer cells. The excellent hydrophobic drug loading capacity of nanoPMOs into the porous structure, and glutathione-triggered controlled drug release properties could improve the effectiveness of highly biodegradable nanoPMOs which exhibit better cancer cell targeting ability in targeted chemotherapy of prostate cancer, resulting in the potent anticancer activity of EAB4H nanorods with low lethal concentrations (LC_{50}).

2. Results and Discussion

2.1. Synthesis and characterization of various nanoPMOs.

Benzene or ethylene-based periodic mesoporous organosilica nanoparticles (nanoPMOs) with variable sizes, shapes, and compositions are synthesized using organosilane precursors (bis(triethoxysilyl)benzene (BTEB), bis(triethoxysilyl)ethene (BTEE), bis(triethoxysilylpropyl)disulfide or tetrasulfide at different molar ratios according to our previous sol-gel protocol with minor modifications (Table S1, Supporting Information).^[22] The fluorescence and redox-responsive biodegradability properties of nanoPMOs are successfully measured by covalently incorporating the optimized amount of Cy3 dye molecules and glutathione-sensitive disulfide or tetrasulfide linkages into the organosilica framework, respectively. The spherical-shaped nanoparticles are consistently obtained using 1,4-bis(triethoxysilyl)benzene (BTEB) as organosilica precursor while the use of 1,2-bis(triethoxysilyl)ethene (BTEE) as organosilica precursor produces nanorods. Cetyltrimethylammonium bromide allows the generation of mesoporous structure, which benefits the nanoPMOs to be efficient drug delivery systems.

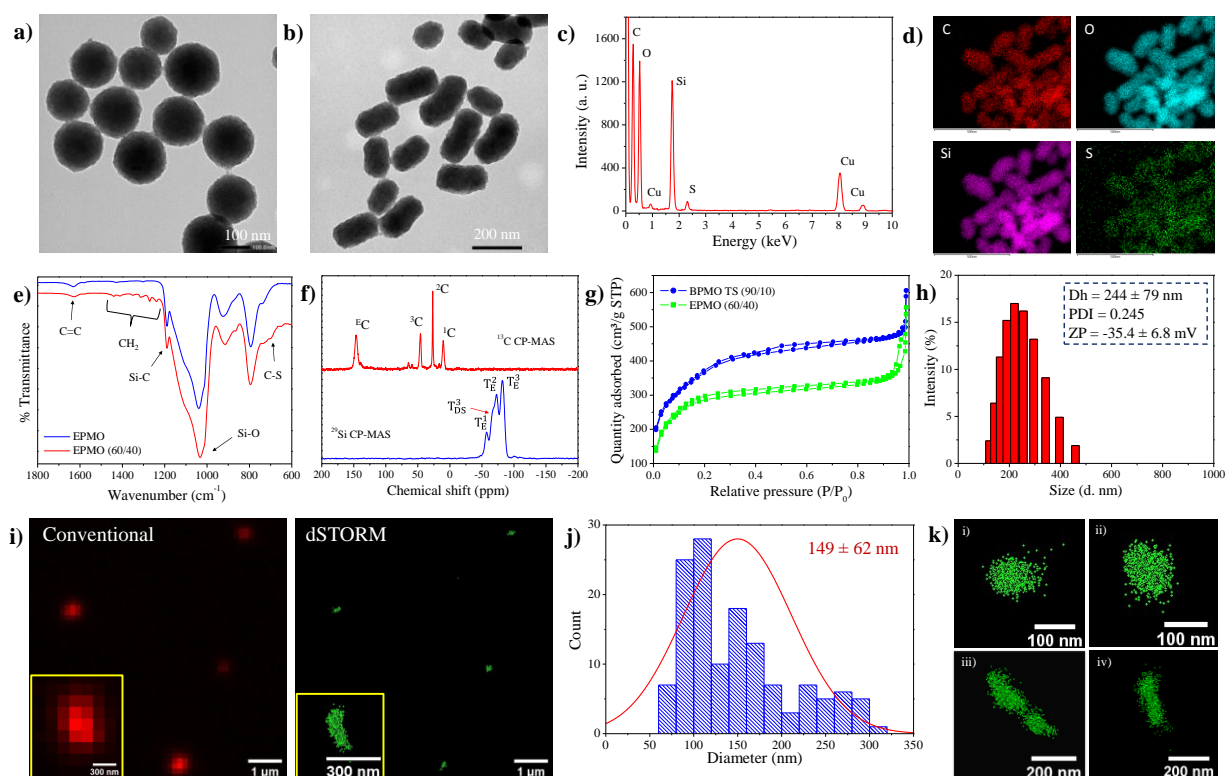


Figure 1. Characterization of fluorescent and biodegradable periodic mesoporous organosilica nanoparticles (nanoPMOs). a, b) Representative TEM images of BPMO TS (90/10) nanosphere and EP MO (60/40) nanorod, respectively. c) Energy dispersive X-ray spectrum (EDS) of BPMO TS (90/10) nanosphere. d) Elemental mapping images of different elements present in the framework of EP MO (60/40) nanorod: carbon (C), oxygen (O), silicon (Si), and sulfur (S). e) ATR-FTIR spectra of EP MO and EP MO (60/40) nanorods. f) Solid-state ^{13}C and ^{29}Si CP-MAS NMR spectra of EP MO (60/40) nanorod. g) Nitrogen adsorption-desorption isotherms of BPMO TS (90/10) nanosphere and EP MO (60/40) nanorod. h) Hydrodynamic size distribution of EP MO (60/40) nanorod measured by dynamic light scattering method. The inset displays the value of the hydrodynamic diameter (Dh), polydispersity index (PDI), and zeta potential (ZP) of the nanorod. i) Conventional microscopy, total internal reflection fluorescence (TIRF) image (left side) of EP MO (60/40) nanorod and their direct stochastic optical reconstruction microscopy (dSTORM) image (right side). The inset shows the corresponding images of a single nanorod. j) The optical size distribution histogram of EP MO (60/40) nanorod with the average size of nanorods as presented in the inset obtained from the dSTORM analysis. k) The dSTORM images of different types of single nanoPMO nanosphere and nanorod: i) BPMO (90/10) nanosphere, ii) BPMO TS (90/10) nanosphere, iii) EP MO (75/25) nanorod, and iv) EP MO (60/40) nanorod.

Transmission electron microscopy (TEM) is initially used to examine the structural properties of these nanoPMOs, mainly their sizes and morphologies. As shown in **Figure 1a,b** and Figure S1-S3, Supporting Information, TEM images of nanoparticles demonstrate the successful production of monodisperse nanoPMO nanospheres as well as nanorods,

depending on the nature of organosilane (BTEB or BTEE respectively) used for the synthesis. According to the size distribution histograms derived from the TEM images of nanoparticles (Figure S1 and S2, Supporting Information), the diameter of nanospheres and the length and width of nanorods vary with the organosilica precursor ratios. The calculated average sizes of these nanoPMOs are summarized in **Table 1** and also presented in the inset of their size distribution histogram (Figure S1 and S2, Supporting Information). As a result of the introduction of disulfide linkages into the framework of nanoPMOs, the average size of spherical nanoPMOs decreases from 197 ± 41 nm to 181 ± 29 nm, while the incorporation of tetrasulfide bonds instead of disulfide results in further reductions. Similarly, the length and width of the nanorods significantly reduce as the disulfide-bridged organosilica precursor, bis(3-triethoxysilylpropyl)disulfide (BTEPDS) concentration increases. Consequently, the aspect ratios of these nanorods are also affected, leading to the production of nanorods of different aspect ratios. For example, the nanorods (EPMO) having no disulfide bonds exhibit an average length of 379 nm and width of 146 nm, resulting in an aspect ratio of 2.54, however, these are reduced to 195 nm and 107 nm, respectively for EPMO (60/40) nanorods with an aspect ratio of 1.79 where 40% BTEPDS are co-hydrolyzed/condensed with BTEE. The hydrodynamic diameter (D_h) of these nanoPMOs with a polydispersity index (PDI) measured by the dynamic light scattering method (Table 1, Figure 1h and Figure S4, Supporting Information) is very consistent with the results obtained from TEM. The low PDI values (<0.3) indicate that nanoparticles are colloidal stable in aqueous solutions without significant aggregation. The zeta potentials of nanoPMOs in aqueous media are in the range of -31 to -36 mV, suggesting their similar negative surface charge (Table 1, and Figure 1h, and Figure S5, Supporting Information) which is attributed to the presence of silanol groups at deprotonated condition.

The successful incorporation of disulfide linkages in the framework of nanoPMOs is confirmed by the presence of sulfur (S) element along with silicon (Si) in the energy dispersive X-ray spectrum (EDS) of BPMO TS (90/10) nanosphere as shown in Figure 1c. The elemental mapping of EPMO (60/40) demonstrates that four major elements, carbon (C), oxygen (O), silicon (Si), and sulfur (S) are uniformly distributed throughout the nanoparticles (Figure 1d). In addition, the approximate amount of each element measured from the corresponding EDS analysis are presented in Table S2, Supporting Information. The chemical structure of nanoPMOs is analyzed by ATR-FTIR spectroscopy and then solid-state NMR. The FTIR spectra of spherical nanoPMOs exhibit their characteristic peaks at 1630 and 1150 cm^{-1} corresponding to C=C, and Si-C bonds, respectively of benzene-bridged organosilica (Figure S6a, Supporting Information). Similarly, the nanoPMO nanorods produced from ethylene-bridged organosilica also have characteristic peaks of C=C, and Si-C bonds at 1630 and 1190 cm^{-1} , respectively (Figure 1e, and Figure S6b, Supporting Information). In addition, the Si-O stretching vibration of benzene- and ethylene-bridged organosilica is shown at 1070 cm^{-1} and 1030 cm^{-1} , respectively. Most importantly, the appearance of additional multiple peaks for C-H stretching vibration at 3000-2850 cm^{-1} and bending vibration at 1500-1200 cm^{-1} of methylene groups confirm the successful incorporation of disulfide or tetrasulfide linkages in the nanoPMOs framework. These peaks become more intense with increasing concentrations of disulfide-bridged organosilane, BTEPDS. Interestingly, a weak C-S band at 695 cm^{-1} is exclusively observed in the case of EPMO (60/40) nanorod where an elevated amount of BTEPDS is used (Figure 1e). In order to confirm the nature of silicon sites present in nanoPMOs, the EPMO (60/40) nanorod is characterized by solid-state ^{29}Si CP-MAS NMR spectroscopy as shown in Figure 1f. The spectrum shows three distinct signals with chemical shifts of -57.3, -72.8, and -82 ppm, corresponding to the T¹, T², and T³ sites, respectively of ethylene-bridged organosilica (designated as T_Eⁿ, n = 1, 2, and 3). Moreover, the chemical

shift at -67 ppm is due to the disulfide-bridged organosilica T³ site (i.e. T_{DS}³). Alternatively, the ¹³C CP-MAS NMR spectrum confirms the presence of propyl moieties of BTEPDS from the signals at 10.5, 26.7, and 45.8 ppm for consecutive three carbons of (-Si-¹CH₂-²CH₂-³CH₂-S-). There is also a main characteristic NMR signal of 146.2 ppm corresponding to the ethylene group (denoted as ^EC). In addition, nitrogen adsorption-desorption analysis is conducted to evaluate the mesoporous structure of nanoPMOs as illustrated in Figure 1g and Figure S7, Supporting Information. A summary of Brunauer-Emmett-Teller (BET) surface areas, pore sizes, and pore volumes determined by Barrett-Joyner-Halenda (BJH) analysis of as-synthesized nanoparticles is presented (Table 1, and Figure S7, Supporting Information). The results show that all nanoPMOs possess type IV isotherm with narrow hysteresis, a large surface area in the range of 950-1550 m²/g and a superior pore volume (0.86-1.47 cm³/g). As well, the nanoparticles have uniform pore diameters varying between 2.5 and 4.1 nm. Notably, EPMO (60/40) nanorod has a significant decrease in surface area and a relatively large pore size that could be attributed to the condensation with BTEPDS.

Next, the super-resolution dSTORM imaging of such as-synthesized fluorescent nanoPMOs labeled with STORM-compatible Cy3 dyes is investigated to understand their structural features (i.e., optical size and shape, and number of localizations per nanoparticle) which are essential to the evaluation of their surface functionality and redox-responsive degradation quantitatively. Since the dSTORM imaging technique has a superior spatial resolution beyond the diffraction limits, compared to conventional fluorescence imaging modalities like total internal reflection fluorescence (TIRF), it allows the nanoparticle's optical structures to be resolved in the nanometer range.^[23] As a result, conventional TIRF images of nanoPMOs fail to reveal their actual structural properties; however, dSTORM imaging readily reveals these characteristics (Figure 1i-k, and Figure S8 and S9, Supporting Information). According to dSTORM imaging, the optical shape of nanoparticles produced is

similar to that acquired by the TEM imaging technique. Although TEM has more resolution, dSTORM imaging is more quantitative. The optical size of nanoPMOs as well as the number of localizations per nanoparticle determined by MatLab analysis of their dSTORM data using the mean shift clustering algorithm ^[20a, 23] are presented in Table 1. Nanospheres and nanorods have smaller optical sizes compared to their actual sizes measured by TEM, indicating that Cy3 dye molecules are most probably distributed at the center rather than on the surface of the nanoparticles. Indeed, we are measuring where the dyes are and how many they are with dSTORM. Therefore, the average optical length of the larger nanorod, EPMO, is 149 nm, which is significantly smaller than the TEM size of around 379 nm. In contrast, the colloidal stable small-sized nanorod, EPMO (60/40) has an average optical length of 145 nm close to the true value of 195 nm. Furthermore, the nanoparticles become smaller as their size decreases, which may result in a gradual decline in localizations per particle (Figure S10, Supporting Information).

Table 1. Various physicochemical properties of fluorescent and biodegradable nanoPMOs used in this study.

nanoPMOs	Shape	Size (nm) [¶] & aspect ratio	Hydrodynamic size (nm) & PDI	Zeta potential (mV)	Optical size [#] (nm)	Surface area (m ² /g)	Pore size (nm)	Pore volume (cm ³ /g)
BPMO	nanosphere	197, ~1	291, 0.184	-33.1	108	1377	2.9	0.99
BPMO (90/10)	nanosphere	181, ~1	274, 0.119	-31.7	107	1465	2.6	1.19
BPMO TS (90/10)	nanosphere	165, ~1	253, 0.115	-34.2	86	1263	2.8	0.94
EPMO	nanorod	379 x 146, 2.54	365, 0.193	-34.1	149	1304	2.9	1.47
EPMO (90/10)	nanorod	329 x 136, 2.39	334, 0.255	-31.4	143	1567	2.7	1.09
EPMO (75/25)	nanorod	292 x 122, 2.37	293, 0.156	-33.6	152	1538	2.5	1.32
EPMO (60/40)	nanorod	195 x 107, 1.79	244, 0.245	-35.4	149	942	4.1	0.86

[¶] Average size of nanoparticles was measured from TEM images.

[#] Average optical size of nanoparticles was calculated from dSTORM analysis.

2.2. Surface functionalization of nanoPMOs.

NanoPMO surfaces are further engineered using two different surface chemistries in order to generate reactive functional groups for the immobilization of anti-M6PR antibodies in two different ways: oriented and non-oriented respectively. The first approach involves the grafting of well-characterized small molecule, Fmoc-protected semicarbazide Silane (Figure S11, Supporting Information) on the surface of nanoPMOs through silanol groups followed by the acid-catalyzed deprotection of the Fmoc group, resulting in the semicarbazide functionalized nanoparticles.^[24] The successful grafting is confirmed by the presence of amide bonds corresponding to the bands around 1650 and 1553 cm^{-1} in ATR-FTIR analysis as shown in Figure 2a, and Figure S12a,b, Supporting Information.^[25] The significantly enhanced fluorescence properties of fluorescamine molecules by semicarbazide functionalized nanoparticles indicate the generation of surface-exposed semicarbazide groups (Figure S13, Supporting Information). In another approach, nanoPMOs are similarly grafted with amino silane on their surface and then functionalized with succinic anhydride to produce carboxylic acid^[26] functionalized nanoparticles. The ATR-FTIR spectra of functionalized nanoPMOs (Figure 2a and Figure S12c, Supporting Information) indicate carboxyl bands in the range of 1685-1745 cm^{-1} , confirming the carboxyl functionalization of nanoPMOs. In both cases, the modification of the surface of nanoPMOs does not alter their intrinsic morphology as shown by TEM (Figure S14, Supporting Information). These two surface modification approaches are therefore successful in preparing various functional nanoPMOs as summarized in Table S3, Supporting Information. Owing to the surface modification of nanoPMOs, the hydrodynamic sizes are slightly increased while the surface charges are significantly altered (i.e., semicarbazide functionalized nanoparticles become more positive, and more negative charge is observed for nanoparticles functionalized with carboxylic acid) as shown in Figure 2b, and Figure S15 and S16, Supporting Information. Moreover, the surface modification approaches have a different impact on the porosity of nanoPMOs, which can further

influence their degradation properties. While the pore diameter remains almost the same as that of pristine nanoparticles, the pore volume (V_p) is decreased in both approaches (Figure S17, Supporting Information). The effect is more pronounced for carboxylic acid functionalized nanoparticles where V_p is reduced from 0.86 to 0.22 cm^3/g thanks to the possibility of amino silane hydrolysis and condensation within pores, as well as the increased weight of nanoparticles following surface functionalization.

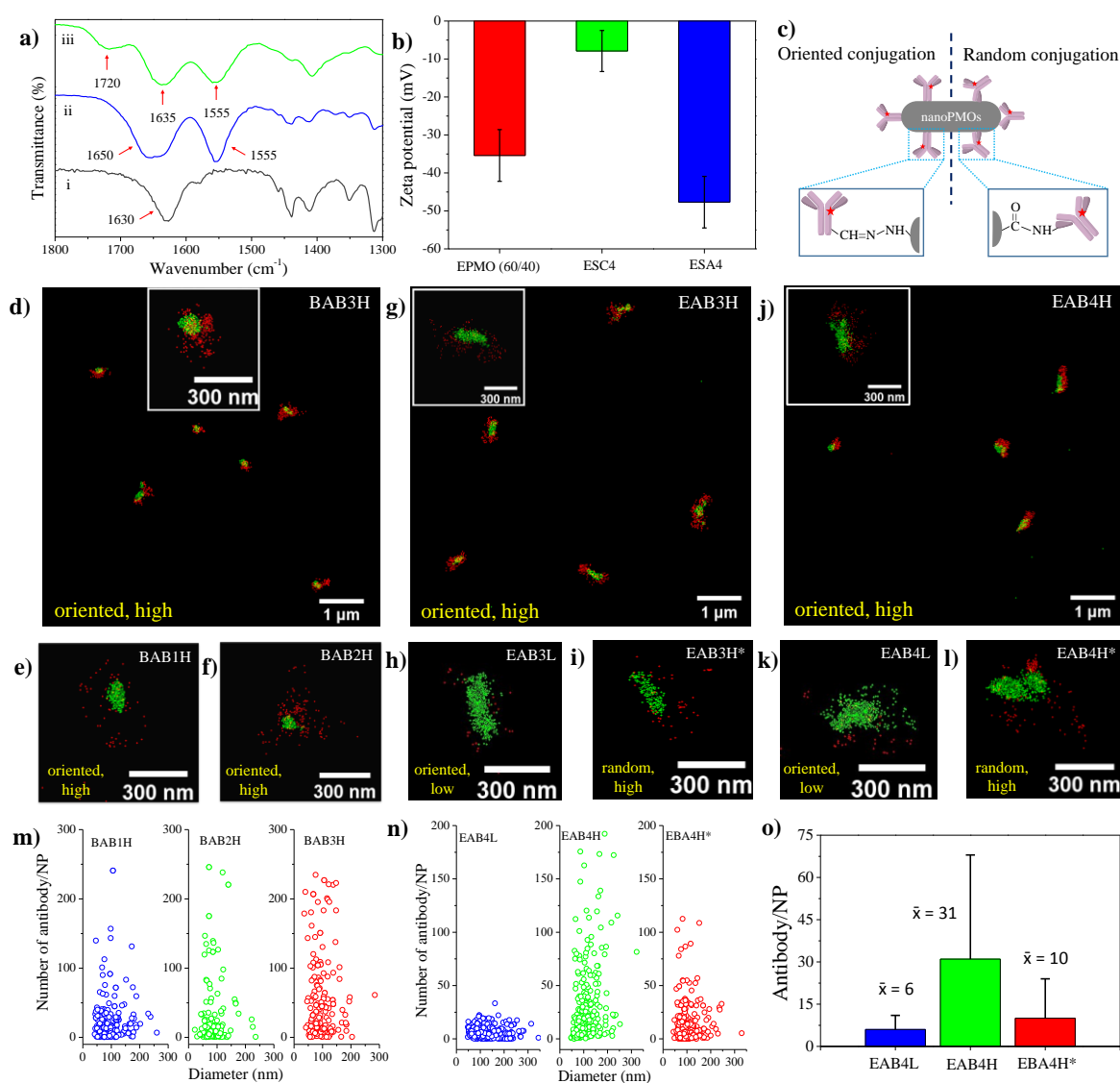


Figure 2. Characterization of surface functionality of BTEE and BTEB-based nanoPMOs. a) ATR-FTIR spectra of i) pristine EPMO (60/40) nanorod, ii) semicarbazide functionalized nanorod (ESC4), and iii) carboxylic acid functionalized nanorod (ESA4). b) The zeta potentials of an aqueous solution of EPMO (60/40) nanorods before and after surface modification using two different surface chemistries. c) A schematic representation of two different routes of conjugating Cy5 dye-labeled anti-M6PR antibody with functionalized nanoPMOs. d) The dSTORM imaging of BSC3 spherical nanoparticles oriented conjugated to the antibody at high density

(BAB3H). e, f) The zoom of dSTORM images of individual antibody conjugated spherical nanoPMOs, BAB1H and BAB2H produced by oriented conjugation, respectively. g) The dSTORM imaging of ESC3 nanorod oriented conjugated to a high number of antibody (EAB3H). h, i) The zoomed-in image of dSTORM of individual ESC3 nanorod conjugated with antibody in an oriented manner at low density (EAB3L) and randomly conjugated with antibody at high density (EBA3H*), respectively. j) The dSTORM imaging of oriented antibody conjugated ESC4 nanorods at high density (EAB4H). k, l) The high magnification dSTORM images of individual ESC4 nanorod conjugated with antibody in an oriented low-density mode (EAB4L) and in a random mode at high density (EBA4H*), respectively. m) The distribution of antibody numbers per nanoparticle of the corresponding antibody conjugated various nanospheres determined by dSTORM analysis. n) The distribution of antibody numbers per nanoparticle of the ESC4 and ESA4 nanorod conjugated with the antibody at different orientations and multivalency determined by dSTORM analysis. o) The average number of antibody per nanoparticle determined by dSTORM analysis of the corresponding antibody conjugated nanorods. In dSTORM images of antibody conjugated nanoPMOs, nanoparticles are presented in green, whereas antibody localizations are displayed in red. The insets display the high magnification dSTORM image, presenting a single antibody conjugated nanoparticle.

Using site-specific or random conjugation techniques, surface-modified nanoPMOs are oriented or randomly conjugated with anti-M6PR antibody, respectively (Figure 2c) to better understand the impact of the orientation of antibody on their targeting capability of prostate cancer cells. The oriented chemical attachment of antibodies to the functionalized nanoparticles is achieved by first oxidizing the carbohydrate residue in the antibody's Fc region into aldehyde groups using periodate-based oxidation, followed by chemical condensation with nanoparticles functionalized with semicarbazide groups. Thus, the oriented anti-M6PR antibodies expose their antigen binding sites (i.e. Fab fragments) towards the outside, making it easier for them to bind to cell surface mannose 6-phosphate receptors (M6PR). In contrast, the carbodiimide-coupling chemistry is employed to chemically conjugate carboxylic acid functionalized nanoPMOs to primary amine groups found in antibodies, including Fab fragments, producing randomly conjugated nanoPMOs containing antibodies immobilized in various spatial directions such as head-on and side-on. Therefore, the poor accessibility of Fab fragments of anti-M6PR antibody may reduce the targeting capability of nanoPMOs toward prostate cancer cells. In this study, we have prepared a series

of shape- and size-tunable nanoPMOs conjugated with anti-M6PR antibody at different orientations and multivalency (Table S4, Supporting Information) to evaluate their prostate cancer cell targeting ability.

To visualize the distribution of anti-M6PR antibody on the surface of nanoPMOs by super-resolution dSTORM imaging technique, the oxidized antibody is chemically conjugated with another STORM-compatible dye, cyanine 5 (Cy5) prior to conjugate with nanoparticles. According to UV-visible absorption spectroscopy of antibody labeled with Cy5 dye, there is approximately one estimated amount of dye per antibody. As a result, each antibody produces an average localization number of 3.9 determined from Cy5 dye blinking events in the calibration of individual fluorescent antibody using single molecule dSTORM imaging ^[20a] as shown in Figure S18, Supporting Information. Next, various anti-M6PR antibody conjugated nanoPMOs at different orientations and multivalency are imaged by dSTORM at identical conditions. It is also possible to determine the number of antibodies immobilized per nanoparticle via quantifying the red-colored localizations corresponding to antibodies by dSTORM data analysis using the mean shift clustering algorithm as previously mentioned. Furthermore, semicarbazide functionalized nanorod (ESC3) is similarly imaged to determine if Cy3 dye blinks falsely in channel 647. There is, however, no significant number of localization in the red channel (Figure S19a, Supporting Information). Carboxylic acid functionalized nanorod (ESA4) incubated with antibody in absence of carboxyl activating agents such as EDC/NHS followed by purification is also imaged to evaluate the nonspecific adsorption of antibody. The dSTORM imaging as shown in Figure S19b, Supporting Information reveals no significant localizations corresponding to the Cy5 dye labeled antibody, indicating less possibility of nonspecific antibodies adsorbing on the surface of nanoPMOs.

Among a variety of functional nanoPMOs, spherical nanoparticles are chemically conjugated with a high concentration of anti-M6PR antibody in an oriented arrangement only. The dSTORM imaging of antibody-conjugated spherical nanoparticles is depicted in Figure 2d-f and Figure S20a,b, Supporting Information, where the spherical nanoparticles appear as green while red localizations corresponding to antibodies, confirming that the antibody is successfully immobilized on nanoparticle surfaces. Next, the conjugation efficiency is evaluated by quantifying the antibody number for each nanoparticle from MatLab analysis of dSTORM data. An analysis of the antibody number per nanoparticle for three different nanoPMOs is presented in Figure 2m in the form of scatter plots. Following that, pie charts illustrate the statistical distribution of nanoparticle populations with a specific number of antibodies per nanoparticle (Figure S21a, Supporting Information). Results show a gradual decline of non-conjugated nanoparticle populations, while antibody-expressing nanoparticle populations (> 50 per nanoparticle) are increasing when the nanoparticle size is reduced. For example, larger-sized BAB1H nanoparticle has around 7% nanoparticles without any antibody whereas this population is reduced to below 4% in the case of BAB3H nanoparticle of small size. As opposed to BAB1H nanoparticle, BAB3H nanoparticle has a higher proportion of nanoparticles conjugated with more than fifty antibodies (38% compared to 11%). Therefore, in the site-specific conjugation approach, the higher antibody conjugation efficiency increases when the size of spherical particles is reduced, resulting in an overall higher number of antibodies conjugated per nanoparticle on average. (Figure S21a, Supporting Information). Antibody conjugation efficiency might be affected by colloidal stability changes in conjugation environments and/or by the surface accessibility of semicarbazide groups on spherical nanoparticles, which is better with small nanoparticles. In addition, the substantial enhancement in hydrodynamic size is observed as shown in Figure

S22, Supporting Information indicating the successful conjugation of antibodies at high density on the surface of the nanoparticles.

Similarly, the successful anti-M6PR antibody conjugation at variable numbers and orientations with four nanoPMO nanorods of different sizes is qualitatively as well as quantitatively characterized by dSTORM imaging and analysis, respectively. Among these nanorods, the larger ones (ESC1 and ESC2) which have comparatively low colloidal stability show low efficiency in oriented antibody conjugation although using highly concentrated antibody (Figure S20c,d, Supporting Information). Due to this, a low number of conjugated antibodies are found in the nanoparticle population, and consequently, conjugated antibodies per nanoparticle are also lower (approximately 14) for these larger nanorods (EAB1H and EAB2H) as displayed in Figure S21b,c, Supporting Information. However, both ESC3 and ESC4 nanorods with comparatively small sizes are more efficient at antibody conjugation under similar reaction conditions as shown in Figure 2g,j. Therefore, the significant higher population of nanoparticles conjugated with high-density antibodies is found in the scatter plots (Figure 2n, and Figure S21d, Supporting Information) and pie charts (Figure S21e,f, Supporting Information), consequently producing a high number of oriented antibody conjugated nanorods (approximately 38 and 31 for EAB3H and EAB4H, respectively) as presented in Figure 2o and Figure S21d, Supporting Information. Additionally, the low number of antibodies are also conjugated to both nanorods by the same conjugation strategy, where five times less anti-M6PR antibody is used. In Figure 2h,k, and Figure S20e,g, Supporting Information, dSTORM imaging of EAB3L and EAB4L nanorods demonstrates that a low number of red localizations surround the nanoparticles, indicating successful conjugation. In agreement with expectations, the number of quantified antibodies is very low for each nanorod (Figure 2n, and Figure S21d, Supporting Information). In this way, it is possible to prepare nanorods that contain as many as five antibodies per nanoparticle as

presented in Figure 2o, and Figure S21d, Supporting Information. In the conjugation with lower antibodies, the smallest EAB4L nanorod shows higher homogeneity than the larger EAB3L nanorod (Figure S21e,f, Supporting Information) which can influence their cellular uptake efficiency. In contrast, dSTORM imaging of carboxylic acid functionalized ESA3 and ESA4 nanorods randomly conjugated with antibody (EBA3H* and EBA4H*) indicates that conjugation efficiency of EDC/NHS coupling chemistry for non-oriented chemical attachment of antibody to nanorods is low in comparison to condensation reactions involving for oriented conjugation (Figure 2i,l, and Figure S20f,h, Supporting Information). As a result, the nanoparticles are mostly located in the region of a low number of antibodies per nanoparticle in scatter plot as shown in Figure 2n, and Figure S21d, Supporting Information. Pie charts in Figure S21e,f, Supporting Information also show that significant percentage of comparatively larger ESA3 nanorod without any antibody (~30%) is found in random antibody conjugation whereas this percentage is approximately 7% for the smallest nanorod (ESA4). Therefore, random antibody attachment also exhibits similar heterogeneity as low-density oriented conjugation of antibodies. A heterogeneous surface functionality of antibody conjugated nanorods may affect their interaction with prostate cancer cells.

2.3. Redox-responsive degradation of nanoPMOs.

The in vitro degradation activities of several nanoPMOs with varied shapes, compositions, and surface chemistries in response to glutathione at different concentrations is qualitatively examined by TEM. For this study, nanoPMOs are incubated at room temperature with phosphate-buffered solution (10 mM, pH 7.4) containing 10 mM and 10 μ M reduced glutathione which mimic intracellular (2-10 mM) and extracellular glutathione (2-10 μ M) level, respectively and subsequently, the morphological changes of nanoPMOs are observed by TEM at different incubation times. At first, the concentrated glutathione-induced degradation of semicarbazide functionalized two spherical nanoPMOs, BSC2 and BSC3

incorporated with an equivalent amount of disulfide and tetrasulfide linkages, respectively are studied as presented in Figure 3a,b and Figure S23-S26, Supporting Information. TEM images demonstrate that the nanosphere undergoes both surface erosion as well as bulk erosion because of the cleavage of disulfide or tetrasulfide linkages by glutathione, leading to progressive degradation into small fragments over time. Interestingly, all nanospheres are not starting to degrade at the same time from the beginning, therefore, a significant number of nanospheres are found as unchanged morphological conditions even after a longer incubation period. As shown in Figure 3a,b, the BSC3 nanosphere having tetrasulfide linkages produce a significantly larger number of small fragments with few unbroken nanospheres in comparison to BSC2 after 6 days of incubation. This indicates that the BSC3 nanosphere is more susceptible to degradation than BSC2 nanoparticles in which disulfide linkages are incorporated.

The in vitro degradation of nanorods incorporating different proportions of disulfide linkages is also evaluated in order to understand the effect of composition on the degradation behavior. Therefore, semicarbazide functionalized nanorods synthesized by using 10%, 25%, and 40% disulfide-bridged organosilica precursor, BTEPDS are imaged by TEM after incubation with 10 mM glutathione solution for different times as shown in Figure 4a-c and Figure S27-S32, Supporting Information. The results show that the production of the degraded small-sized fragments is gradually increased at a longer incubation time (i.e. 6 days) with increasing the disulfide contents^[27] in the framework of nanoPMOs (Figure 4a-c), which is in sharp contrast with previous studies,^[10a] showing that the surface functionalization has a dramatic effect on the degradation rate of the nanoPMOs. Additionally, the number of nanorods with a morphology similar to primary nanorods is significantly reduced. Time-dependent in vitro degradation analysis reveals that high-incorporated disulfide linkages, which are cleaved by glutathione, enhance degradation rates. Accordingly, ESC4 nanorods

have high degradation properties, whereas ESC2 has low degradation properties at higher glutathione concentrations. It is also observed that spherical nanoparticles, BSC2 are more degradable compared to nanorods, ESC2 where an equivalent amount of BTEPDS are used for synthesis (Figure 3a and 4a). The degradation of nanorods is also influenced by the surface modification approaches used for the preparation of functional nanoparticles. Figure 4c,d and Figure S31-S34, Supporting Information demonstrate that semicarbazide functionalized nanorods (ESC4) degrade more rapidly than nanorods functionalized with carboxylic acid groups (ESA4). This is possibly attributed to the significant reduction in the pore volume of ESA4 nanorods. Furthermore, TEM images at higher magnification (Figure S28, S30, S32, and S34, Supporting Information) reveal possible mechanisms underlying mesoporous nanorod degradation. In addition to the surface erosion caused by external glutathione, the diffused glutathione extensively cleaves the disulfide network in the core, creating a hollow structure that further breaks into different-sized fragments. In contrast, all biodegradable nanoPMOs retain their pristine structure after 6 days of exposure to glutathione solution at a low concentration (10 μ M) as shown in Figure S35 and S36, Supporting Information, indicating no significant effect of extracellular glutathione on their chemical structure. Since the quantitative analysis of nanoPMOs degradation by TEM is more challenging, therefore we explore for the first time a single molecular super-resolution dSTORM imaging technique.

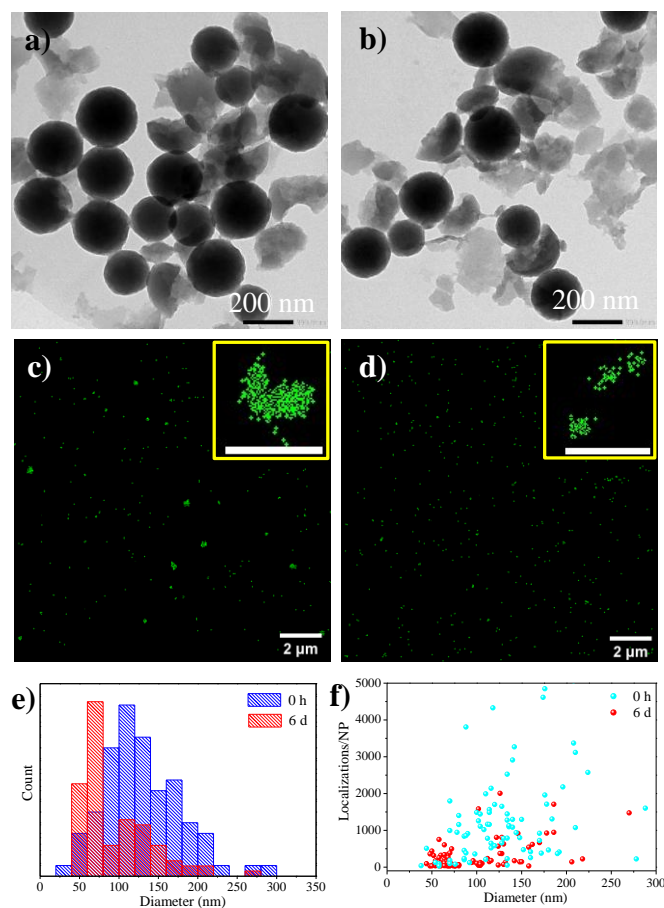


Figure 3. a, b) Representative TEM images and c, d) dSTORM images of biodegradable spherical BSC2 and BSC3 nanoPMOs, respectively after incubation with 10 mM glutathione in phosphate buffer (10 mM, pH 7.4) for 6 days. The inset of dSTORM images shows the corresponding individual degraded nanoparticles or small fragments. The scale bars are 200 nm. e) The optical size distribution histogram and f) scatter plot of BSC3 nanoparticles after 0 hour and 6 days of incubation with a phosphate-buffered solution containing 10 mM glutathione represent the variation of nanoparticle's optical size as well as the number of localization per nanoparticle owing to the glutathione-responsive degradation.

The glutathione-triggered degradation of various surface functionalized nanoPMOs is then visualized and quantified using super-resolution dSTORM imaging. The degradation is qualitatively assessed by observing the diffusion of localizations corresponding to Cy3 dye molecules incorporated into nanoPMOs. In contrast, to quantify the degradation, changes in the optical diameter and number of localizations per nanoparticle over time are determined using MatLab analysis as mentioned earlier. It is observed in dSTORM imaging as presented

in Figure 3c,d and Figure S37, S38, Supporting Information that the highly degradable BSC3 nanosphere as evaluated by TEM produces smaller and/or ultrasmall fragments with fewer localizations than the BSC2 nanosphere, leading to spreading of Cy3 dye localizations in dSTORM imaging frame over time. Consequently, the optical size of BSC3 nanoparticles is gradually decreased, which is more significant after long-term incubation (Figure 3e and Figure S39a,b, Supporting Information). After 6 days of incubation, the average optical size of the BSC2 nanosphere reduces from 131 nm to 105 nm while the BSC3 nanosphere shows a reduction from 129 nm to 93 nm. Besides, Figure 3f and Figure S39c, Supporting Information show that the localization number per nanoparticle is also reduced throughout the degradation process due to the generation of ultrasmall fragments up to the molecular level which can not be observed by low-resolution TEM as well as the breaking of nanoPMOs into various small-sized fragments confirmed by TEM. A significant reduction in localization number for both nanoparticles at an early stage (i.e., 1 day) where optical sizes remain unaffected indicates that diffused glutathione dissolve the nanoparticle's core (Figure S39c, Supporting Information). Further breaking of nanoparticles into small-sized fragments also reduces the localizations for each nanoparticle which is more prominent at 6 days incubation for BSC3 nanosphere where optical size is significantly reduced (Figure 3f and Figure S39c, Supporting Information). Thus, dSTORM analysis reveals that tetrasulfide linkages cleave more rapidly than disulfide linkages, leading to a higher degradation of the BSC3 nanosphere. As illustrated in Figure S40, Supporting Information, their chemical structure is highly stable in glutathione solution at a low concentration (10 μ M), resulting in no significant changes in their optical size distribution as compared to pristine one.

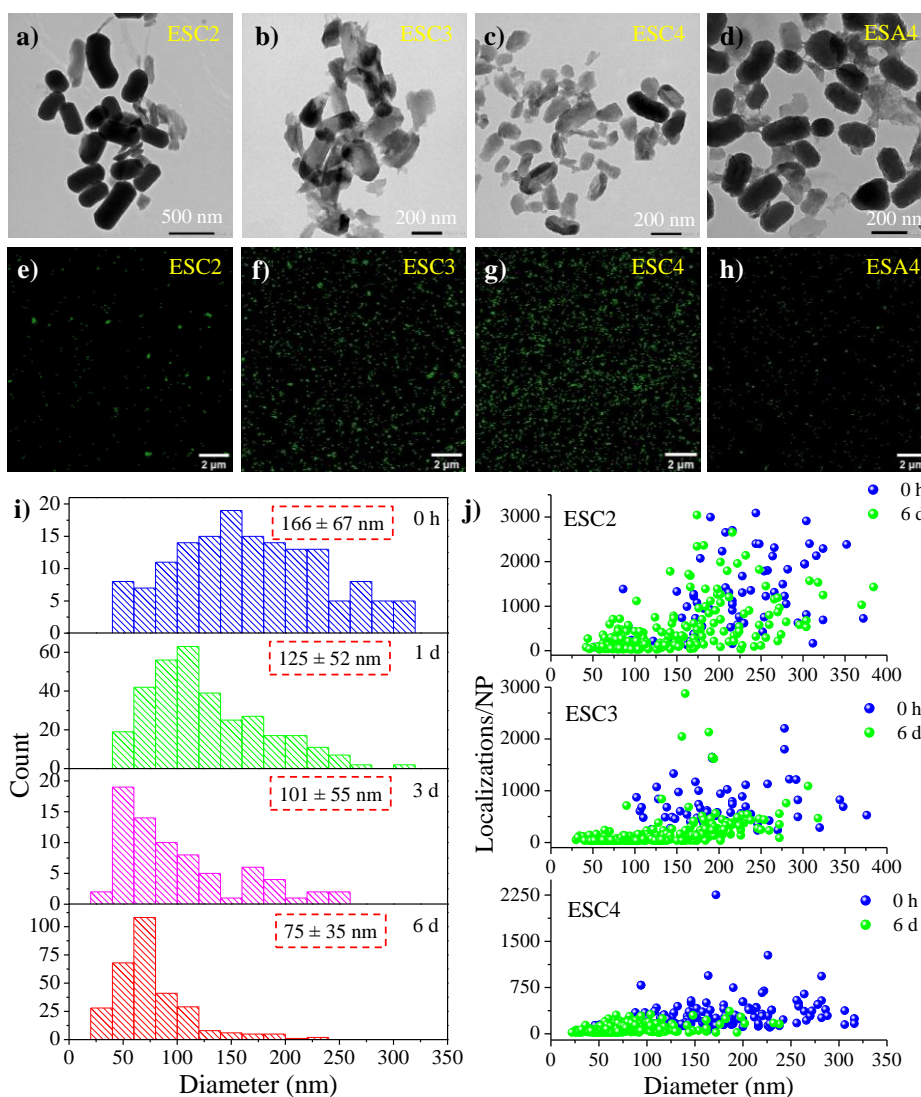


Figure 4. a-d) Representative TEM images and e-h) dSTORM images of different biodegradable nanoPMOs nanorods with varied size, composition, and surface chemistry incubated with 10 mM glutathione solution in phosphate buffer (10 mM, pH 7.4) for 6 days. i) The optical size distribution histogram of ESC4 nanorod after different time incubation with a phosphate-buffered solution containing 10 mM glutathione measured by dSTORM analysis. The inset display the calculated average optical diameter of degraded nanorods. j) The distribution of localization number per nanoparticle as presented in the scatter plots for different nanorods at an early stage (i.e. 0 h) and late stage (i.e. 6 d) of incubation with 10 mM glutathione solution.

Using the dSTORM imaging technique, we also investigate and quantify the degradation behavior of various nanoPMO nanorods with different surface functionalization when incubated in reduced glutathione solution at a high concentration (10 mM) for different time periods. The dSTORM imaging of time-dependent degradation of semicarbazide

functionalized nanorods containing varied extents of glutathione-sensitive disulfide linkages in the framework is shown in Figure S41-S43, Supporting Information, indicates that the degradation increases over time and its rate depends on the disulfide level present in the nanoparticles. Therefore, ESC4 nanorods with a high quantity of disulfide linkages become faster than ESC2 and ESC3 nanorods with a low quantity of disulfide, resulting in an increased localization of Cy3 in the frame of dSTORM imaging after 6 days of incubation (Figure 4e-g). Consequently, Figure 4i,j, and Figure S44, Supporting Information demonstrate that as nanorods degrade, their optical size and localization number as quantified by MatLab analysis gradually decrease over time and disulfide quantity significantly influences the extent of reduction. For instance, ESC2, ESC3, and ESC4 nanorods have a reduction of the optical size of 27.5%, 36.4%, and 54.8%, respectively whereas their localization number is subsequently reduced to 53.5%, 74.6%, and 72.1%, respectively after 6 days of incubation. Hence, the degradation rate of nanoPMOs is controlled by the number of disulfide linkages incorporated into the framework. As a result, ESC4 nanorods which have a high content of disulfide bonds degrade faster, whereas the presence of low disulfide bonds in ESC2 nanorods slow their degradation. Similarly, the influence of surface chemistry on the degradation as observed by TEM is also analyzed by dSTORM imaging (Figure 4h and Figure S45, Supporting Information). As compared to nanorods with semicarbazide chemistry (ESC3 and ESC4), succinic acid functionalized nanorods (ESA3 and ESA4) have a low degradation rate in presence of glutathione where pore volume is low, leading to a less reduction in optical diameter (Figure S46, Supporting Information). Furthermore, the degradation of antibody conjugated nanorod (EAB4H) is also slow because of partial blocking of pores by antibodies (Figure S46 and S47, Supporting Information). Therefore, the surface chemistry that affects the porosity of nanoPMOs affects their degradation properties. On the other hand, glutathione at low concentrations does not significantly affect the physical and chemical structures of

nanorods for up to six days as shown in Figure S48, Supporting Information. As a result, the glutathione-triggered excellent biodegradability of nanoPMOs especially BSC3 nanosphere and ESC4 nanorod is very supportive for intracellular glutathione responsive drug delivery where the toxicity of prematurely released chemotherapeutics can be avoided.

2.4. Biocompatibility and cell imaging.

To evaluate the application potentiality of various functional nanoPMOs in the biomedical field as drug delivery systems, the biocompatibility of these nanoparticles is measured by PrestoBlue cell viability assay. ^[28]The *in vitro* cytotoxicity of these nanoparticles is quantified after 24 h incubation of pre- and post-conjugated nanoparticles with antibody at varied nanoparticle concentrations (2.5-100 µg/mL) with human prostate cancer LNCaP cells and human healthy prostate cell line RWPE-1 (Figure S49 and S50, Supporting Information). The results show that all nanoparticles have more than 80% cell viability in both cell lines up to highest dose, suggesting excellent biocompatibility of nanoparticles.

The next step is to quantify the ability of an array of non-conjugated and antibody-conjugated nanoPMOs to label prostate cancer LNCaP cells using flow cytometry. The cell binding capability of nanoPMOs is significantly influenced by their physicochemical properties such as size, shape, and surface chemistry as shown in Figure S51, Supporting Information. Among non-conjugated nanoparticles, nanoPMO nanorods have comparatively higher nonspecific uptake than spherical-shaped nanoPMOs, mainly driven by the aspect ratio and colloidal stability of nanoparticles. ^[29] Accordingly, highly colloidal stable ESA3 nanorods with an aspect ratio of 2.37 exhibit higher nonspecific interactions than ESA4 nanorods with similar surface functionality which have a low aspect ratio of 1.79 (Figure S51a, Supporting Information). In contrast, anti-M6PR antibody conjugation with nanoPMOs allow them to target M6PR overexpressed prostate cancer cell, depending on their

morphological and surface functional properties (Figure S51b, Supporting Information). Interestingly, there are no significant changes in cellular uptake of antibody conjugated spherical nanoPMOs whereas comparatively smaller-sized nanorods have higher cell labeling aptitude. Most importantly, the orientation and density of conjugated antibodies have a potential impact on the cell-targeting ability of particular nanoPMOs. The oriented antibody conjugated nanorods show better targeting capacity than nanorods conjugated with antibody randomly anchored owing to the higher accessibility of antigen binding Fab fragments of oriented antibody. As a result, the prostate cancer cell's labeling ability of both EAB3H and EAB4H nanorods where antibodies are conjugated in an oriented way at high density is significantly enhanced by 5-6 times (Figure S51, Supporting Information). The cell labeling capability of oriented antibody conjugated nanorods at low density (EAB4L) is also similar, whereas the heterogeneous surface functionality of EAB3L nanorods reduces the binding capacity to 1.25 times despite both having comparable multivalency. Conversely, random antibody conjugation in EBA4H* nanorods with multivalency close to EAB4L nanorods shows two times lower cell labeling efficiency due to poor accessibility of Fab fragments.

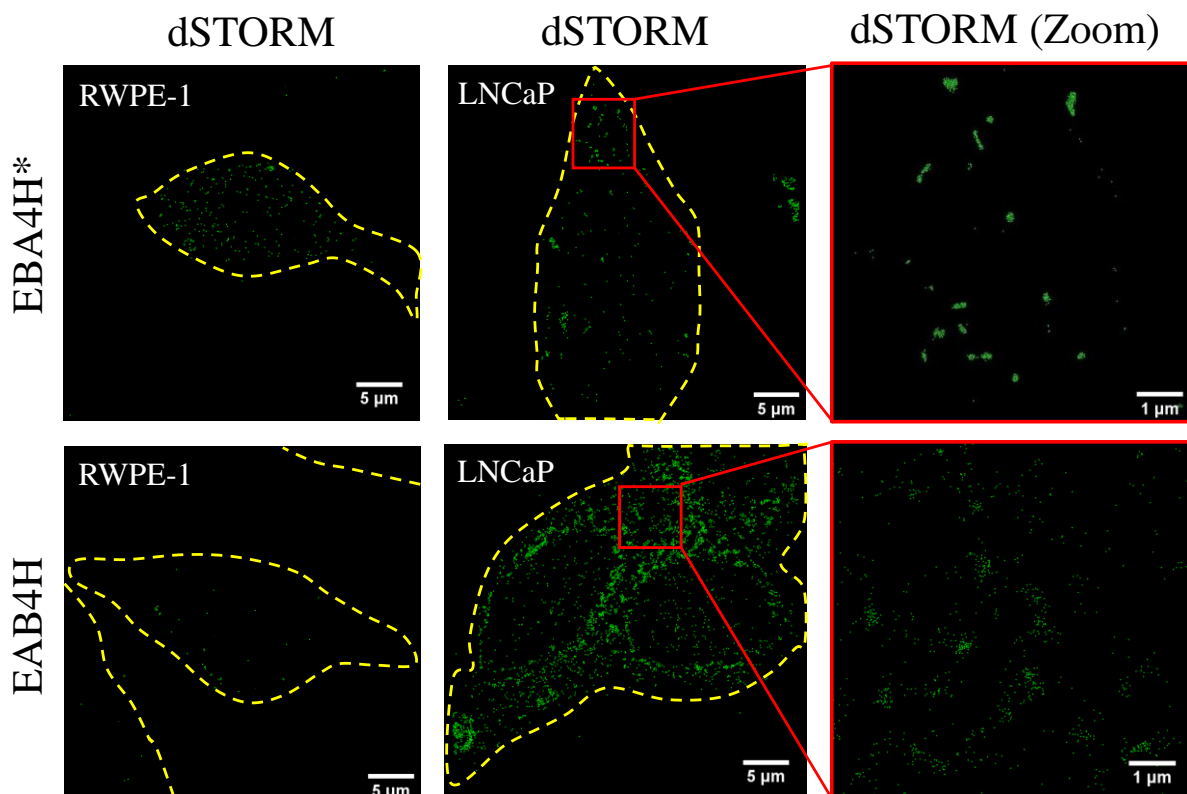


Figure 5. The dSTORM imaging of healthy prostate RWPE-1 cells and prostate cancer LNCaP cells labeled with randomly anti-M6PR antibody conjugated ESA4 nanorod (EBA4H*) and oriented anti-M6PR antibody conjugated ESC4 nanorod (EAB4H) after 6 h incubation at a final nanoparticle concentration of 6 $\mu\text{g}/\text{mL}$.

In order to monitor the localization of biodegradable nanoPMOs and their degradation behavior in the cells, the dSTORM imaging of both prostate cancer and healthy cells is implemented with selected nanoparticles that exhibit better in vitro biodegradation properties in response to the concentrated glutathione, and higher cell targeting capability. Therefore, antibody conjugated nanorods EAB4H and EBA4H* and their non-conjugated counterparts ESC4 and ESA4 are mainly incubated with prostate cancer LNCaP and healthy RWPE-1 cells at a concentration of 6 $\mu\text{g}/\text{mL}$ for 6 h. Figure 5, and Figure S52, Supporting Information show that nanorods conjugated to the anti-M6PR antibody are more efficiently localized intracellularly of M6PR overexpressed LNCaP cells compared to non-conjugated nanorods as a result of the antibody's interaction with cell surface receptors. The time-dependent cellular uptake of EAB4H nanorods by LNCaP cells as presented in Figure S53, Supporting Information indicates that a significant number of nanorods remain attached to the cell membrane after 1 h of incubation and migrate inside the cells over time, particularly after 6 h incubation period. As determined by the diffuse blinking of Cy3 dye molecules incorporated into nanorods, dSTORM imaging in zoom mode also demonstrates that elevated glutathione levels (2-10 mM) in intracellular space significantly induce the degradation of EAB4H nanorods (Figure 5) and the consequent release of Cy3. Moreover, the EAB4H nanorod has low nonspecific cellular uptake by healthy RWPE-1 cells, signifying less nonspecific toxicity to the surrounding healthy prostate cells/tissues (Figure 5). Thus, an intracellular stimuli-responsive biodegradable nanorod conjugated with antibody in an oriented manner (EAB4H) showing excellent cancer cell targeting ability and low nonspecific interaction properties is

very crucial as a responsive drug delivery platform for targeted effective chemotherapy of prostate cancer.

2.5. Drug loading and release studies, and in vitro anticancer activity.

Three anticancer drug molecules with different structural features (e.g. 5-fluorouracil, gemcitabine hydrochloride, and doxorubicin hydrochloride) are utilized in order to assess the drug loading capacity of various functional nanoPMOs. The loading of drugs into the mesoporous structure of nanoparticles is primarily executed at physiological pH by using 10 mM phosphate buffer (pH 7.4). Table S5, Supporting Information, summarizes the drug encapsulation efficiency and loading content of various functional nanoPMOs which are determined by the calibration curve of drugs (Figure S54, Supporting Information). In comparison to the smaller hydrophilic drugs 5-fluorouracil (5-FU) and gemcitabine (GEM), which exist in the form of neutral molecules at pH 7.4, positively charged hydrophobic doxorubicin (DOX) is more efficient for loading into functional nanoparticles. The presence of hydrophobic moieties such as benzene or ethylene in the framework of nanoPMOs facilitates higher DOX loading through strong π - π stacking and hydrophobic interactions. Furthermore, the electrostatic interaction and hydrogen bonding between functional groups of nanoPMOs (e.g. silanol, semicarbazide, and carboxyl) and DOX improve the drug loading efficiency. Consequently, both nanoPMOs functionalized with semicarbazide and carboxyl groups have higher DOX encapsulation efficiency as well as loading content (Table S5, Supporting Information). Due to the higher pore volume, semicarbazide functionalized nanoparticles enable to encapsulation of more drug molecules compared to nanoparticles containing carboxyl groups. It is estimated that approximately 86.8% of DOX is encapsulated in the mesoporous organosilica framework of ESC4 nanorods, which have a typical DOX loading capacity of 30.4% as shown in Figure 6a. While the encapsulation efficiency of the ESA4 nanorod is reduced to 83.9%, resulting in a lower drug loading capacity of 29.3%

(Figure 6a). However, the drug loading aptitude of these nanorods is significantly decreased when the loading is done with 10 mM acetate buffer at pH 5 (Figure 6a, and Table S5, Supporting Information). This is likely the result of the weak interactions and bonding between nanorods and DOX owing to the higher drug solubility and the protonation of nanorod functional groups at acidic pH levels. Furthermore, the UV-visible absorption spectrum of antibody conjugated nanoPMO nanorods (EAB4H) illustrates that DOX is significantly loaded into ESC4 nanorods after antibody conjugation at physiological pH (Figure S55, Supporting Information). However, the drug encapsulation efficiency (~82.1%) and loading content (~28.7%) have been slightly lowered compared to non-conjugated nanorods possibly thanks to the partial blocking of pores by antibodies.

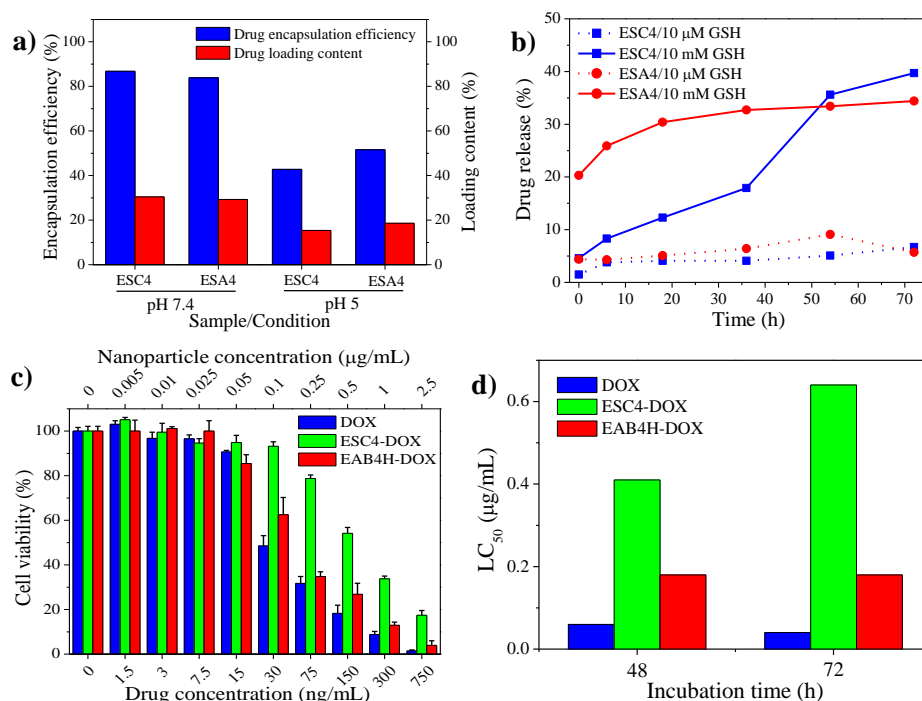


Figure 6. a) The anticancer drug doxorubicin encapsulation efficiency and loading capacity of functionalized nanoPMO nanorods containing semicarbazide groups (ESC4) and carboxyl groups (ESA4) at different pH. b) In vitro drug release profiles of doxorubicin loaded ESC4 and ESA4 nanorods exposed to different concentrations of glutathione solution at pH 7.4. c) In vitro cytotoxicity of free DOX, DOX loaded ESC4 nanorods, and DOX loaded EAB4H nanorods after 72 h incubation with human prostate cancer LNCaP cells at different nanoparticle and drug concentrations. Data are presented as mean \pm SD of three independent experiments. d) The lethal concentration 50 (LC₅₀) values of free DOX, DOX loaded ESC4 nanorods, and DOX loaded EAB4H nanorods as determined after 48 and 72 h of incubation with LNCaP cells.

Next, we have investigated the glutathione responsive drug release properties of various DOX loaded functional nanoPMOs at different concentrations of glutathione and pH. The release of DOX is generally studied at room temperature in phosphate buffer solution (10 mM, pH 7.4) containing 10 μ M and 10 mM glutathione after a certain time in the range of 0-72 h. There is negligible drug release up to 72 h of exposure to low glutathione levels (i.e. 10 μ M), where nanoPMO structures are not susceptible to degradation (Figure 6b, and Figure S56, Supporting Information). The amount of drug released from nanoPMOs functionalized semicarbazide is quantified to be < 7%, whereas the amount is increased up to ~10% for carboxyl functionalized nanoPMOs after 72 h of incubation. Such comparatively high premature DOX release from nanoPMOs with surface-exposed carboxyl groups (e.g. ESA3 and ESA4) indicates the partial adsorption of DOX on the external surface or close to the entrance of pores. As a result, low premature release of DOX can be expected in extracellular environments where the GSH level is 2-20 μ M. Conversely, DOX loaded biodegradable nanoPMOs release drug molecules at a higher rate at elevated GSH levels via breaking the disulfide or tetrasulfide linkages present in nanoPMOs. Therefore, higher amounts of released DOX up to 40% are found after 72 h incubation of nanoparticles in the solution of 10 mM GSH at pH 7.4, which is in good agreement with the degradation nature of nanoPMOs by the same concentrated GSH. Note that, a burst drug release of both ESA3 and ESA4 nanorods occurs at an early stage within 12 h, as compared to those functionalized with semicarbazide groups like ESC3 and ESC4. There is a possibility that drug molecules might be present near the pore entrance or on the exterior surface of ESA3 and ESA4 nanorods, which are released by GSH-induced surface erosion, while ESC3 and ESC4 nanorods encapsulate DOX inside the porous structure near the nanoPMOs center. Accordingly, Figure 6b shows that ESC4 nanorods have a slow drug release performance in the beginning, which is then boosted by the

GSH-induced bulk degradation over time. Moreover, the release of drug from ESA4 nanorod becomes rapid when the medium is acidic in nature (pH 5), while no significant changes are observed in the release profile of ESC4 nanorod as shown in Figure S57, Supporting Information. This is possibly due to the weakness of electrostatic interaction between nanorods and DOX by protonation of carboxylate at pH 5. Therefore, oriented antibody conjugated ESC4 nanorod (i.e. EAB4H) with higher biodegradability, drug loading and controlled release capacity, and prostate cancer cell targeting ability are very effective for potent targeted chemotherapy of prostate cancer.

To elucidate the chemotherapeutic effect of DOX present in different formulations toward prostate cancer cells, the cell viability of LNCaP cells treated with them at various concentrations for 24-72 h is determined by the typical MTT assay. As shown in Figure 6c, and Figure S58 and S59 in Supporting Information, free DOX, nanorods, DOX loaded ESC4 nanorods (ESC4-DOX), and EAB4H nanorods loaded with DOX (EAB4H-DOX) all exhibit cell toxicity against prostate cancer LNCaP cells depending on dosages, incubation times, and formulations. Due to passive diffusion mediated higher cellular uptake of free DOX by LNCaP cells, it becomes more cytotoxic than once loaded into nanorods, leading to low lethal concentrations (LC_{50}) of 60 and 40 ng/mL for 48 and 72 h incubation, respectively (Figure 6d). There is, however, a major issue with nonspecific toxicity caused by free DOX in cancer chemotherapy.^[3] In contrast, the toxicity of DOX present in biodegradable nanorods is significantly influenced by their cellular uptake process and drug release behavior. In spite of the fact that ESC4 nanorods have a greater payload of DOX and a higher degradation rate than EAB4H nanorods, EAB4H-DOX appear to have stronger anticancer activity because of their effective active targeting of M6PR overexpressed prostate cancer cells by the oriented conjugated anti-M6PR antibody (Figure 6c). The highly accumulated EAB4H-DOX nanoparticles by receptor-mediated endocytosis mostly localized in cell cytoplasm release a

significant quantity of DOX and consequently exhibit better cancer cell killing capability. The relatively low cytotoxicity of ESC4-DOX is observed as a result of nonspecific uptake by cancer cells. For instance, the cancer cells treated with ESC4-DOX at a nanoparticle concentration of 0.25 $\mu\text{g}/\text{mL}$ which is equivalent to 75 ng/mL drug concentration show almost 79% viable cells after 72 h incubation, while this value is reduced to 35% when treated with EAB4H-DOX at the same nanoparticle concentration in which DOX concentration is relatively low (ca. 70 ng/mL) as displayed in Figure 6c. As a result, EAB4H-DOX shows a low LC_{50} of 0.18 $\mu\text{g}/\text{mL}$ containing DOX at a concentration of ca. 52 ng/mL after 72 h treatment while ESC4-DOX has a comparatively higher LC_{50} of 0.64 $\mu\text{g}/\text{mL}$ containing DOX at a concentration of ca. 192 ng/mL (Figure 6d).

3. Conclusions

Here, we have introduced a single molecule and super-resolution microscope technique, dSTORM to optimize the physicochemical properties of highly emerged biocompatible as well as biodegradable periodic mesoporous organosilica nanoparticles (nanoPMOs) as an effective drug delivery system for targeted and responsive chemotherapy of prostate cancer. The high spatial resolution at the nanoscale level (around 20 nm) of dSTORM imaging successfully allows for resolving the structural properties such as optical size and shape of various synthesized and well-characterized fluorescent nanoPMOs. The qualitative and quantitative measurements of reduced glutathione-activated degradation of nanoPMOs incorporated with disulfide or tetrasulfide linkages by dSTORM imaging demonstrate their structural properties dependent degradation behavior, overcoming the limitations of the most frequently used TEM measurement. The nanoPMO nanospheres containing tetrasulfide bonds become more susceptible to degradation than equivalent quantities of disulfide incorporated

spherical nanoPMOs, while the degradation rates increase gradually as the number of disulfide bonds in the framework of nanoPMO nanorods increases. The uniform mesoporous structure of nanoPMOs allows the loading of chemotherapeutic molecules and subsequently their biodegradability properties induced by concentrated glutathione control the drug release profile. In contrast, single molecule imaging of the dSTORM technique enables to characterize the surface functionality of various anti-M6PR antibody conjugated nanoPMOs at a single nanoparticle level which show a significant impact along with other physicochemical properties such as size and shape on M6PR overexpressed prostate cancer cells targeting. It has been found that small-sized nanoPMO nanorods conjugated with oriented antibody (EAB4L) have a greater prostate cancer cell labeling ability than spherical nanoPMOs having similar surface functionality (BAB2H and BAB3H), and randomly conjugated nanorods with similar multivalency (EBA4H*). Furthermore, nanorods with high multivalency, especially large nanorods (EAB3H), which are homogeneously coated with antibodies, are more effective at targeting prostate cancer cells. Conversely, large nanorods with low multivalency (EAB3L) have heterogeneous surface functionality, which reduces cell targeting efficacy. As a result, the anticancer drug doxorubicin-loaded extremely biodegradable and small-sized nanoPMO nanorods conjugated with the oriented antibody at high density (EAB4H-DOX) effectively deliver the drug molecules to cancer cells because of its greater selective cellular uptake by cancer cells and subsequent responsive drug release properties triggered by intracellular glutathione, resulting in effective chemotherapy of prostate cancer with lower lethal concentrations (LC₅₀).

4. Experimental Section

Synthesis of periodic mesoporous organosilica nanoparticles (nanoPMOs).

Several fluorescent and biodegradable periodic mesoporous organosilica nanoparticles were synthesized via our previous method with minor alterations.^[22] Briefly, 686 μmol

cetyltrimethylammonium bromide (250 mg) was dissolved in 120 mL distilled water and then 875 μ L aqueous solution of NaOH (2 M) was added in a 250 mL round bottom flask. The solution was heated at 80 °C for 50 min under the stirring condition at 1000 rpm. Next, the mixture of different organosilane molecules at varied quantities was added to the reaction solution dropwise (Table S1, Supporting Information). The reaction was continued for 2 h at 80 °C and cooled to room temperature. Next, cetyltrimethylammonium bromide (CTAB) was removed from nanoparticles using an ethanolic solution of NH_4NO_3 (6 g/L) and the nanoparticles were washed with ethanol, water, and ethanol, respectively (see Supporting Information for detail). Finally, the purified fluorescent nanoPMOs were dispersed in ethanol and were stored at 2-8 °C in a dark environment.

Synthesis of semicarbazide functionalized nanoPMOs. The nanoPMOs were functionalized with semicarbazide groups using the following protocol. In brief, 60 mg nanoPMOs dispersed in 3 mL ethanol (96%) were mixed with 10 μ L triethylamine followed by a 2 mL ethanol solution containing 200 mg Fmoc-Silane. The reaction mixture was stirred at 80 °C for 18 h in the dark. After that, 10 μ L piperidine was added for Fmoc deprotection and the reaction was further continued for 30 min under identical conditions. The nanoparticles were washed four times with ethanol and then with distilled water. The nanoparticles was collected via centrifugation at 20000 rpm for 10 min. Finally, purified semicarbazide functionalized nanoPMOs were dispersed in Milli-Q water and stored at 2-8 °C.

Synthesis of carboxylic acid functionalized nanoPMOs. The nanoPMOs were functionalized with carboxylic acid via the following two steps. In the first step, 60 mg nanoPMOs were mixed with 100 μ L (3-aminopropyl)triethoxysilane in 5 mL ethanol (96%), followed by 18 h of stirring at 80 °C in the dark. The (3-aminopropyl)triethoxysilane grafted nanoparticles were then separated by centrifugation at 20000 rpm for 10 min. The

nanoparticles were washed with ethanol three times and collected via centrifugation under the same conditions. The nanoPMOs functionalized with amine groups were completely dried at room temperature under a vacuum. Nanoparticles were dispersed in 4 mL of anhydrous DMF and a solution of succinic anhydride (200 mg) in anhydrous DMF (2 mL) was added to the nanoparticle's solution in the next step. The reaction mixture was stirred under dark conditions at room temperature overnight. The carboxylic acid-functionalized nanoparticles were collected and then washed three times with distilled water in order to purify them. A similar centrifugation technique was used to collect the nanoparticle pellet. Finally, purified nanoPMOs functionalized with carboxylic acid were dispersed in Milli-Q water and then stored at 2-8 °C.

Antibody conjugation. The oriented conjugation of anti-M6PR antibody with nanoPMOs was performed via the most common condensation reaction between semicarbazide groups of nanoparticles and aldehyde groups present on the oxidized antibody. In brief, approximate 20 or 4 pmol Cy5 labeled anti-M6PR antibody in phosphate buffer solution (pH 7.4, 10 mM) was mixed with semicarbazide functionalized nanoPMOs (0.5 mg) and then the mixture was stirred for 6 h at room temperature in the dark. Next, antibody conjugated nanoparticles were collected via centrifugation at 13000 rpm for 10 min and subsequently washed several times with 10 mM phosphate buffer pH 7.4. The purified antibody conjugated nanoparticles were finally dispersed in Milli-Q water (500 μ L) and stored at 2-8 °C.

For random conjugation of anti-M6PR antibody with nanoparticles, two steps carbodiimide-based coupling reaction was utilized. At first, 0.5 mg carboxylic acid functionalized nanoPMO nanorods were dispersed in 10 mM MES buffer (pH 5.5) and then 5 nmol 1-ethyl-3-(3-dimethylaminopropyl)carbodiimide hydrochloride and 100 nmol N-hydroxysuccinimide were added to the nanoparticle's solution. The mixture was stirred for 45 min at room temperature to activate the carboxylic groups of nanoparticles. The nanoparticles

with activated carboxyl groups were collected via centrifugation at 13000 rpm for 12 min. Subsequently, the nanoparticles were dispersed in 10 mM phosphate buffered solution (pH 7.4) containing approximate 20 pmol Cy5 labeled anti-M6PR antibody and incubated in the dark for 6 h under a stirring condition for the reaction between primary amine groups of antibody and activated carboxyl groups of nanoparticles. Next, antibody conjugated nanoparticles were washed several times with phosphate buffer (10 mM, pH 7.4) and dispersed in 500 μ L Milli-Q water. Finally, the aqueous solution of nanoparticles conjugated with antibody was stored at 2-8 $^{\circ}$ C.

Monitoring the degradation of nanoPMOs by TEM. The glutathione-responsive degradation of various functionalized nanoPMOs was evaluated in phosphate buffered solution of 10 μ M and 10 mM reduced glutathione. Briefly, 0.5 mg semicarbazide functionalized nanoparticles or carboxylic acid functionalized nanoparticles was dispersed in 10 mM phosphate buffer pH 7.4 (5 mL) with different concentrations of glutathione (10 μ M and 10 mM). The resulting nanoparticle solution was stirred at room temperature under an ambient atmosphere. At different incubation time points (up to 7 days), aliquots (200 μ L) were taken and diluted with one mL Milli-Q water. The diluted solution was used to visualize the nanoparticle's degradation by transmission electron microscope (TEM).

dSTORM imaging of nanoPMOs and antibody conjugated nanoPMOs. For dSTORM imaging of nanoPMOs and antibody conjugated nanoPMOs, the flow chambers with an approximate volume of 30-40 μ L were initially constructed by attaching a coverslip on a glass microscopy slide using double-sided scotch tape. To immobilize the nanoparticles on the coverslip, 40 μ L phosphate buffered solution (10 mM, pH 7.4) of nanoparticles at a concentration of 100 μ g/mL was placed into the chamber and then incubated for 10 min. Next, the unbound nanoparticles were washed with dSTORM buffer solution consisting of 5% (w/v) glucose, 10 mM cysteamine, glucose oxidase (0.56 mg/mL) and catalase (34 μ g/mL) in

10 mM PBS solution (pH 7.4) three times. Subsequently, the flow chambers were filled with dSTORM buffer solution and sealed with transparent nail polish. The nanoparticles labeled with Cy3 dye were imaged by acquiring 30000 frames at 10 ms exposure time under 561 nm laser excitation with 100% laser power. In addition to this, 20000 frames of fluorescence signal from Cy5 dye labeled antibody was consequently acquired using 647 nm laser at 75% laser power excitation for antibody conjugated nanoparticles.

Evaluation of nanoPMOs degradation by dSTORM. To evaluate the degradation of nanoPMOs by reduced glutathione, the semicarbazide functionalized nanoparticles or carboxylic acid functionalized nanoparticles (50 μg) was initially incubated in 500 μL phosphate buffered solution of glutathione (10 mM, pH 7.4) with different concentrations (10 μM and 10 mM) under stirring condition for different times. After different time points, the resulting nanoparticles solution (40 μL) at a concentration of 100 $\mu\text{g}/\text{mL}$ was placed into the flow chamber and then allowed to stand for 10 min in order to immobilize them on coverslips. Next, dSTORM buffer solution was used to wash and then fill the flow chambers, and subsequently, the chambers were sealed with transparent nail polish. For dSTORM imaging, the fluorescence signals of Cy3 dye were collected in 30000 frames at 10 ms exposure time under 561 nm laser excitation at 100% laser power. In contrast, a 647 nm laser at 75% laser power was used to excite Cy5 dye and their fluorescence signals were similarly recorded in 20000 frames.

Loading of anticancer drugs. The anticancer drug molecules were loaded into the porous structure of nanoPMOs by mixing nanoparticles (1 mg) with the drug (350 μg) in 500 μL phosphate buffer (10 mM, pH 7.4) or acetate buffer (10 mM, pH 5). The mixture was stirred at room temperature overnight under a dark condition. To remove the free drug, drug-loaded nanoPMOs were collected via centrifugation (13000 rpm, 12 min) followed by washing four times with Milli-Q water. The amount of unloaded drug was quantified by measuring the

absorbance of the supernatant. Finally, the drug-loaded nanoparticles were dispersed in Milli-Q water and stored at 2-8 °C. The loading content (LC) of drug into nanoparticles was calculated using the equation: loading content (%) = (weight of drug loaded into nanoparticles/weight of nanoparticles) X 100. In contrast, drug encapsulation efficiency (EE) of nanoparticles was determined using an equation of encapsulation efficiency (%) = (weight of drug loaded/ weight of drug used) X 100.

Responsive drug release. The glutathione responsive drug release study was carried out in 10 mM phosphate buffer (pH 7.4) or acetate buffer solution (pH 5) containing 10 μM and 10 mM reduced glutathione. Typically, 50 μL doxorubicin loaded nanoPMOs (1 mg/mL) were mixed with glutathione solution (450 μL) and then stirred at room temperature for different times. The released doxorubicin was collected via centrifugation at 13000 rpm for 20 min. The amount of released doxorubicin at different time points was determined via measuring the absorbance of the supernatant at 490 nm. The quantification of drug release was performed by the formula: drug release (%) = (amount of released drug/amount of loaded drug) X 100.

Cell culture. Human prostate cancer LNCaP cells were cultured in RPMI-1640 medium supplemented with 10% fetal bovine serum and 1% penicillin-streptomycin. In contrast, human healthy prostate cell line RWPE-1 was cultivated in keratinocyte-SFM serum free medium supplemented with human recombinant epidermal growth factor and bovine pituitary extract and also 1% penicillin-streptomycin. Both cells were grown in a humidified atmosphere at 37 °C with CO₂. After 70-80% cell confluency, trypsin-EDTA was used to detach the cells for subculture.

Cell viability assay. In vitro cytotoxicity of nanoparticles was measured by the PrestoBlue cell viability assay. Briefly, LNCaP and RWPE-1 cells (~10000 cells/well) were seeded into 96-well flat bottom tissue culture plate using a 100 μL cell culture medium and then incubated for 24 h at 37 °C with 5% CO₂. Afterward, the cells were treated with nanoparticles

at different concentrations in the range of 2.5-100 µg/mL for 24 h. The cells without any treatment were considered as a negative control. Next day, the culture medium containing free nanoparticles was removed from the wells. After that, 100 µL PrestoBlue reagent (10%, v/v) in the fresh culture medium was added to each well followed by incubation for 2 h at 37 °C. The absorbance (A) of the resulting solutions was measured at 570 and 600 nm using a Tecan Infinite M200 PRO multimode microplate reader. Each nanoparticle at the same concentration was tested in triplicate. The cell viability was calculated by the following equation.

$$\text{Cell viability (\%)} = \frac{(A_{570} - A_{600})_{\text{sample}}}{(A_{570} - A_{600})_{\text{control}}} \times 100$$

The results were presented as a mean ± standard deviation.

Flow cytometry. The interaction of various nanoPMOs functionalized with and without antibody with prostate cancer LNCaP cells was quantitatively evaluated using a flow cytometry analysis. LNCaP cells were seeded in a 12-well plate at a density of 10⁵ cells/well and left to grow for 48 h at 37 °C with 5% CO₂. After, the cells were treated with different nanoparticles at a final concentration of 50 µg/mL and incubated for 6 h. After being washed twice with PBS solution, cells were trypsinized, then collected in a culture medium, and centrifuged for 5 min at 1300 rpm. Next, the cell pellets were suspended in 200 µL PBS solution containing MgCl₂ and CaCl₂ and kept on ice until the measurement. The flow cytometry was performed using a NovoCyte flow cytometer and the data were analyzed by NovoExpress software (ACEA Biosciences, Inc.). The evaluation of the nanoparticle internalization was carried out in 20,000 events. The experiment was repeated twice.

dSTORM imaging of cells. Both prostate cancer LNCaP cells and healthy RWPE-1 cells were seeded into µ-slide 8 well glass bottom chambered coverslip at a density of 10000 cells per well with 300 µL cell culture medium and then allowed to grow the cells at a condition of 37 °C with 5% CO₂. Next, the cells were treated with different types of nanoparticles at a

concentration of 6 $\mu\text{g/mL}$ and subsequently incubated for different times (1-6 h). After incubation, the cells were washed with PBS solution (10 mM, pH 7.4) three times to remove free nanoparticles mainly. The washed cells were then fixed via incubating the cells with 4% paraformaldehyde solution at room temperature for 15 min. After three washes with PBS solution, the fixed cells were stored with PBS solution at 2-8 $^{\circ}\text{C}$. For dSTORM imaging of cells, PBS solution was replaced by dSTORM buffer solution (200 μL). The fluorescence signal of Cy3 dye labeled nanoparticles was collected in 30000 frames at 10 ms exposure time under excitation of 561 nm laser with 100% laser power. Subsequently, 20000 frames of fluorescence signal from Cy5 dye attached with antibody was acquired using 647 nm laser at 75% laser power excitation.

In vitro anticancer activity. The MTT assay was performed in order to access the cytotoxicity of free doxorubicin (DOX), nanoPMOs, and DOX loaded nanoPMOs toward prostate cancer cells. For the cytotoxicity study, we seeded 10^4 LNCaP cells per well and incubated them for 24 h in 96-well plates. After that, the cells were treated with DOX, nanoparticles, and DOX loaded nanoparticles at different levels of drug concentration (0-750 ng/mL), or nanoparticle concentration (0-2.5 $\mu\text{g/mL}$) and incubated for a variety of times (1, 2, and 3 days). Cells treated with the vehicle were considered as control. After washing the cells with PBS solution, MTT solution was added to the cells at a final concentration of 0.5 mg/mL, and the cells were incubated for 4 h at 37 $^{\circ}\text{C}$. The produced purple formazan crystals were dissolved in a mixture of ethanol and DMSO (1:1, v/v %). The absorbance (A) of the resulting solutions was measured using Multiskan Sky Microplate Spectrophotometer (Thermo Fisher Scientific) at 540 nm. Finally, the percentage (%) of viable cells was calculated from the following equation: cell viability = $(A_{\text{sample}}/A_{\text{control}}) \times 100$. A dose-response curve of cell viability versus the log of concentration was used to determine the lethal concentration (LC_{50}) value.

Supporting Information

Supporting Information is available from the Wiley Online Library or from the author.

Acknowledgments

This research work is financially supported by the MANTARGET project of Marie Skłodowska-Curie Individual Fellowships (Project No.: 887089) under Horizon 2020 Framework program. The authors would like to acknowledge Erwan Oliviero from the MEA platform, University of Montpellier, for acquiring energy-dispersive X-ray spectroscopy and elemental mapping of nanoPMOs. The authors also acknowledge Cristina Izquierdo Lozano, Eindhoven University of Technology, The Netherlands, and Teodora Andrian, Institute for Bioengineering of Catalonia (IBEC), Spain for helping in the MatLab analysis of dSTORM data, and also Madhura Murar, IBEC, Spain for her assistance in cell culture. P.D. also acknowledges European Commission for Marie Skłodowska-Curie Individual Fellowships.

Conflict of Interest

The authors declare no conflict of interest.

References

- [1] R. L. Siegel, K. D. Miller, H. E. Fuchs, A. Jemal, *CA: a cancer journal for clinicians* **2022**, *72*, 7-33.
- [2] a) L. Wang, L. Lankhorst, R. Bernards, *Nature Reviews Cancer* **2022**, *22*, 340-355; b) *Nature Cancer* **2021**, *2*, 245-246.
- [3] K. Nurgali, R. T. Jagoe, R. Abalo, *Frontiers in pharmacology* **2018**, *9*, 245.
- [4] a) M. J. Mitchell, M. M. Billingsley, R. M. Haley, M. E. Wechsler, N. A. Peppas, R. Langer, *Nat. Rev. Drug Discov.* **2021**, *20*, 101-124; b) T. Briolay, T. Petithomme, M.

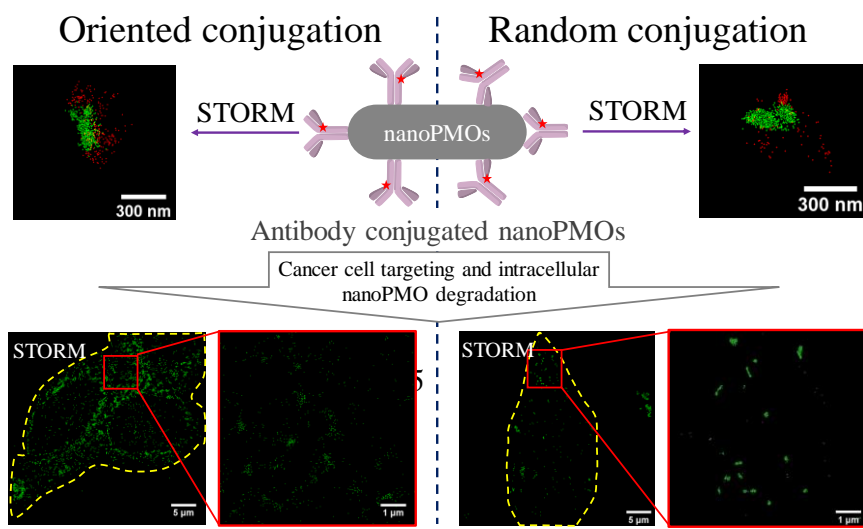
- Fouet, N. Nguyen-Pham, C. Blanquart, N. Boisgerault, *Molecular Cancer* **2021**, *20*, 55.
- [5] a) S. Sindhwani, A. M. Syed, J. Ngai, B. R. Kingston, L. Maiorino, J. Rothschild, P. MacMillan, Y. Zhang, N. U. Rajesh, T. Hoang, J. L. Y. Wu, S. Wilhelm, A. Zilman, S. Gadde, A. Sulaiman, B. Ouyang, Z. Lin, L. Wang, M. Egeblad, W. C. W. Chan, *Nat. Mater.* **2020**, *19*, 566-575; b) D. Rosenblum, N. Joshi, W. Tao, J. M. Karp, D. Peer, *Nature Commun.* **2018**, *9*, 1410.
- [6] J. Bourquin, A. Milosevic, D. Hauser, R. Lehner, F. Blank, A. Petri-Fink, B. Rothen-Rutishauser, *Adv Mater* **2018**, *30*, e1704307.
- [7] a) Y. Arun, R. Ghosh, A. J. Domb, *Adv. Funct. Mater.* **2021**, *31*, 2010284; b) H. Zhou, J. Ge, Q. Miao, R. Zhu, L. Wen, J. Zeng, M. Gao, *Bioconjug. Chem.* **2020**, *31*, 315-331.
- [8] M. A. Rahim, N. Jan, S. Khan, H. Shah, A. Madni, A. Khan, A. Jabar, S. Khan, A. Elhissi, Z. Hussain, H. C. Aziz, M. Sohail, M. Khan, H. E. Thu, *Cancers* **2021**, *13*, 670.
- [9] a) X. Wang, X. Zhong, J. Li, Z. Liu, L. Cheng, *Chem. Soc. Rev.* **2021**, *50*, 8669-8742; b) G. Yang, S. Z. F. Phua, A. K. Bindra, Y. Zhao, *Adv. Mater.* **2019**, *31*, 1805730.
- [10] a) K. Wang, X. Li, H. Wang, H. Lu, D. Di, Q. Zhao, S. Wang, *Colloids and Surfaces A* **2021**, *608*, 125566; b) L. Guan, J. Chen, Z. Tian, M. Zhu, Y. Bian, Y. Zhu, *VIEW* **2021**, *2*, 20200117; c) V. Poscher, Y. Salinas, *Materials* **2020**, *13*, 3668; d) R. S. Guimarães, C. F. Rodrigues, A. F. Moreira, I. J. Correia, *Pharmacol. Res.* **2020**, *155*, 104742; e) S. Chinnathambi, F. Tamanoi, *Pharmaceutics* **2020**, *12*, 890; f) Y. Cheng, X. Jiao, W. Fan, Z. Yang, Y. Wen, X. Chen, *Biomaterials* **2020**, *256*, 120191; g) X. Du, F. Kleitz, X. Li, H. Huang, X. Zhang, S.-Z. Qiao, *Adv. Funct. Mater.* **2018**, *28*,

- 1707325; h) J. G. Croissant, Y. Fatieiev, N. M. Khashab, *Adv. Mater.* **2017**, *29*, 1604634.
- [11] A. K. Pearce, R. K. O'Reilly, *Bioconjug. Chem.* **2019**, *30*, 2300-2311.
- [12] E. Mirhadi, M. Mashreghi, M. Faal Maleki, S. H. Alavizadeh, L. Arabi, A. Badiie, M. R. Jaafari, *Int J Pharm* **2020**, *589*, 119882.
- [13] M. Wang, W. Liu, Y. Zhang, M. Dang, Y. Zhang, J. Tao, K. Chen, X. Peng, Z. Teng, *J. Coll. Int. Sci.* **2019**, *538*, 630-637.
- [14] O. Vaillant, K. El Cheikh, D. Warther, D. Brevet, M. Maynadier, E. Bouffard, F. Salgues, A. Jeanjean, P. Puche, C. Mazerolles, P. Maillard, O. Mongin, M. Blanchard-Desce, L. Raehm, X. Rebillard, J.-O. Durand, M. Gary-Bobo, A. Morere, M. Garcia, *Angew. Chem., Int. Ed.* **2015**, *54*, 5952-5956.
- [15] A. J. Sivaram, A. Wardiana, C. B. Howard, S. M. Mahler, K. J. Thurecht, *Adv Healthc Mater* **2018**, *7*.
- [16] A. A. Saei, M. Yazdani, S. E. Lohse, Z. Bakhtiary, V. Serpooshan, M. Ghavami, M. Asadian, S. Mashaghi, E. C. Dreaden, A. Mashaghi, M. Mahmoudi, *Chem. Mater.* **2017**, *29*, 6578-6595.
- [17] I. Gessner, *MRS bulletin* **2021**, *46*, 643-649.
- [18] a) A. A. Patil, M. J. N. Descanzo, J. B. A. Agcaoili, C.-K. Chiang, C.-L. Cheng, H.-C. Chang, W.-P. Peng, *ACS Applied Nano Materials* **2021**, *4*, 8922-8936; b) S. Okyem, O. Awotunde, T. Ogunlusi, M. B. Riley, J. D. Driskell, *Bioconjug. Chem.* **2021**, *32*, 1753-1762; c) K. Tripathi, J. D. Driskell, *ACS Omega* **2018**, *3*, 8253-8259.
- [19] a) L. Woythe, N. B. Tito, L. Albertazzi, *Adv Drug Deliv Rev* **2021**, *169*, 1-21; b) J. Shang, X. Gao, *Chem. Soc. Rev.* **2014**, *43*, 7267-7278.

- [20] a) L. Woythe, P. Madhikar, N. Feiner-Gracia, C. Storm, L. Albertazzi, *ACS Nano* **2022**, *16*, 3785-3796; b) E. Archontakis, L. Woythe, B. van Hoof, L. Albertazzi, *Nanoscale Advances* **2022**, *4*, 4402-4409.
- [21] a) W. Li, G. S. Kaminski Schierle, B. Lei, Y. Liu, C. F. Kaminski, *Chem. Rev.* **2022**, *122*, 12495-12543; b) S. Dhiman, T. Andrian, B. S. Gonzalez, M. M. E. Tholen, Y. Wang, L. Albertazzi, *Chemical Science* **2022**, *13*, 2152-2166; c) M. Lelek, M. T. Gyparaki, G. Beliu, F. Schueder, J. Griffié, S. Manley, R. Jungmann, M. Sauer, M. Lakadamyali, C. Zimmer, *Nature Reviews Methods Primers* **2021**, *1*, 39.
- [22] J. Croissant, X. Cattoen, M. Wong Chi Man, A. Gallud, L. Raehm, P. Trens, M. Maynadier, J.-O. Durand, *Adv. Mater.* **2014**, *26*, 6174-6178.
- [23] D. van der Zwaag, N. Vanparijs, S. Wijnands, R. De Rycke, B. G. De Geest, L. Albertazzi, *ACS Appl. Mater. Interfaces*. **2016**, *8*, 6391-6399.
- [24] A. Gallud, D. Warther, M. Maynadier, M. Sefta, F. Poyer, C. D. Thomas, C. Rouxel, O. Mongin, M. Blanchard-Desce, A. Morere, L. Raehm, P. Maillard, J. O. Durand, M. Garcia, M. Gary-Bobo, *RSC Adv.* **2015**, *5*, 75167-75172.
- [25] E. Secret, K. Smith, V. Dubljevic, E. Moore, P. Macardle, B. Delalat, M.-L. Rogers, T. G. Johns, J.-O. Durand, F. Cunin, N. H. Voelcker, *Adv. Healthc. Mater.* **2013**, *2*, 718-727.
- [26] J. Zhang, M. Niemelä, J. Westermarck, J. M. Rosenholm, *Dalton Trans.* **2014**, *43*, 4115-4126.
- [27] S. Quignard, S. Masse, G. Laurent, T. Coradin, *Chem. Commun.* **2013**, *49*, 3410-3412.
- [28] M. I. A. Pereira, G. Pereira, C. A. P. Monteiro, C. Geraldés, P. E. Cabral Filho, C. L. Cesar, A. A. de Thomaz, B. S. Santos, G. A. L. Pereira, A. Fontes, *Sci Rep* **2019**, *9*, 2341.

- [29] a) N. Zheng, J. Li, C. Xu, L. Xu, S. Li, L. Xu, *Artif Cells Nanomed Biotechnol* **2018**, *46*, 1132-1140; b) C. Graf, Q. Gao, I. Schütz, C. N. Noufele, W. Ruan, U. Posselt, E. Korotianskiy, D. Nordmeyer, F. Rancan, S. Hadam, A. Vogt, J. Lademann, V. Haucke, E. Rühl, *Langmuir* **2012**, *28*, 7598-7613; c) H. Meng, S. Yang, Z. Li, T. Xia, J. Chen, Z. Ji, H. Zhang, X. Wang, S. Lin, C. Huang, Z. H. Zhou, J. I. Zink, A. E. Nel, *ACS Nano* **2011**, *5*, 4434-4447.

Table of Contents



This study evaluates the most critical properties (e.g. surface functionality and degradation) of highly emerged drug delivery systems known as periodic mesoporous organosilica nanoparticles (nanoPMOs) conjugated with antibodies at different orientations and multivalency by single molecule super-resolution dSTORM technique for effective prostate cancer chemotherapy. NanoPMOs with optimized properties promotes cancer cell targeting and degradation, exhibiting potent anticancer activity.